Mon. Not. R. Astron. Soc. **000**, 1–10 (2006) Printed 4 February 2008 (MN LATEX style file v2.2)

WFCAM, Spitzer-IRAC and SCUBA observations of the massive star forming region DR21/W75: II. Stellar content and star formation

M.S.N. Kumar[1], C.J. Davis[2], J. M. C. Grave[1,5], B. Ferreira[3] & D. Froebrich[4]
[1] *Centro de Astrofsica da Universidade do Porto, Rua das Estrelas s/n 4150-762 Porto, Portugal*
[2] *Joint Astronomy Centre, 660 North A'ohōkū Place, University Park, Hilo, Hawaii 96720, USA.*
[3] *Department of Astronomy, University of Florida, Gainesville, FL 32611-2055, USA*
[4] *Dublin Institute for Advanced Studies, 5 Merrion Square, Dublin 2, Ireland*
[5] *Departamento de Matematica Aplicada da Faculdade de Ciências da Universidade do Porto, Portugal*

arXiv:astro-ph/0610105v1 4 Oct 2006

ABSTRACT
Wide field near-infrared observations and Spitzer Space Telescope IRAC observations of the DR21/W75 star formation regions are presented. The photometric data are used to analyse the extinction, stellar content and clustering in the entire region by using standard methods. A young stellar population is identified all over the observed field, which is found to be distributed in embedded clusters that are surrounded by a distributed halo population extending over a larger projected area. The Spitzer/IRAC data are used to compute a spectral index value, α, for each YSO in the field. We use these data to separate pure photospheres from disk excess sources. We find a small fraction of sources with α in excess of 2 to 3 (plus a handful with $\alpha \sim 4$), which is much higher than the values found in the low mass star forming region IC348 ($\alpha \leqslant 2$). The sources with high values of α spatially coincide with the densest regions of the filaments and also with the sites of massive star formation. Star formation is found to be occuring in long filaments stretching to few parsecs that are fragmented over a scale of $\sim$1 pc. The spatial distribution of young stars are found to be correlated with the filamentary nebulae that are prominently revealed by 8μm and 850 μm observations. Five filaments are identified that appear to converge on a center that includes the DR21/DR21(OH) regions. The morphological pattern of filaments and clustering compare well with numerical simulations of star cluster formation by Bate et al. (2003).

Key words: stars:formation – ISM:HII regions – infrared: stars – turbulence

1 INTRODUCTION

Wide-field near-infrared (NIR) and mid-infrared (MIR) surveys are potentially very useful for mapping the distribution of young stars in Giant Molecular Clouds (GMCs). In particular, the launch of the Spitzer Space Telescope has brought about a revolution in such studies, and several nearby, low-mass star forming regions have been analysed recently (ex Jorgensen et al. 2006; Harvey et al. 2006). With the advent of wide-field imagers on mid-sized, ground based telescopes like the U.K. Infrared Telescope (UKIRT), the deeper near infrared data can be effectively combined with the Spitzer Space telescope observations and the techniques employed on nearby low mass cores can then be applied to relatively distant (d$\sim$2–3 kpc), high-mass star forming regions.

Two such regions are DR21 and W75N in the Cygnus X HII complex. Traditionally observed separately, DR21 and W75N are associated with massive, dense cores separated by about half a degree on the sky (Wilson & Mauersberger 1990; Shirley et al. 2003). Both sources are associated with ultra-compact HII regions (Haschick et al. 1981; Cyganowski et al. 2003), water, OH and/or methanol masers (Plambeck & Menten 1990; Hunter et al. 1994; Torrelles et al. 1997; Kogan & Slysh 1998), and extremely massive bipolar outflows (Moore et al. 1991; Garden et al. 1991; Davis & Smith 1996; Shepherd, Testi & Stark 2003). DR21(OH), a third site of massive star formation, lies $\sim 3'$ north of DR21. Although it too is associated with intense maser activity (Kogan & Slysh 1998; Mangum, Wooten & Mundy 1992), unlike DR21, it is not detected at radio wavelengths and its bipolar outflow is not seen in H_2 emission. All these regions are bright at Far-Infrared (FIR) wavelengths; DR21 is estimated to have an FIR luminosity of $1.5{\times}10^5 L_\odot$ and the W75 region 5-8$\times 10^4 L_\odot$ (Harvey et al. 1977; Campbell et al. 1982).

DR21(OH) probably harbours multiple sources at a younger stage of evolution. DR21 and DR21(OH) coincide with just two peaks in a chain of molecular cores, traced in molecular line and submillimeter continuum emission, that extends north-south over at least 12′ (Chandler, Gear & Chini 1993; Vallée & Fiege 2006). Keto (1990) found collapse signatures in two of the main protostellar condensations coinciding with the UCHII regions DR21 and DR21 D and estimated masses of 270$M_\odot$ and 20$M_\odot$ respectively. All of the above suggest that DR21/W75N is a region with intense massive star formation activity.

The DR21/W75 region has recently been observed with Spitzer and the wide-field camera, WFCAM, at UKIRT. An overview of the Spitzer IRAC and MIPS data has been given by Marston et al. (2004); Smith et al. (2005) and Persi, Tapia & Smith (2006) examine the MIR photometry of the massive, embedded young stars associated with just the DR21 and W75N cores, respectively. The WFCAM observations have been presented by Davis et al. (2006, hereafter Paper I), where narrow-band images in H_2 1-0S(1) emission have been used to search for outflows and jets across a $0.8^\circ \times 0.8^\circ$ field. In Paper I the Spitzer/IRAC photometry is used to search for candidate outflow sources; an 850 μm mosaic is also presented, which traces the W75N cloud and the chain of very young (possibly pre-stellar) star-forming cores running through DR21 and DR21(OH). A colour image showing the field observed with Spitzer is shown here in Fig. 1, along with contours of the 850 μm dust continuum emission, for reference. The relationship between the many outflows, the embedded young stars, the UCHII regions, masers and molecular cores is discussed in some detail in Paper I. In this paper – Paper II – we step back and take a more global view of DR21/W75: the Spitzer/IRAC photometry and UKIRT/WFCAM JHK data are used to characterize and map the distribution of young stars across the field. We derive extinction maps, surface-density maps, and plot colour-colour and colour-magnitude diagrams for some 43,000 WFCAM sources and 1580 Spitzer targets. We use these results to study the nature of the clustered and distributed populations, and their relationship to dense cores, filaments, and the locations of massive stars.

DR21 and W75N are associated with clouds with average Local Standard of Rest (LSR) velocities of $\sim$-3km s^{-1} and $\sim$+9km s^{-1}, respectively; a small amount of foreground gas at $V_{\rm LSR} \sim +9$km s^{-1} may also lie in front of DR21. Dickel et al. (1978) propose that the DR21 and W75N cores are interacting, based on their modest-resolution mapping and an observed velocity gradient across W75. However, in our higher-resolution 850 μm maps in Paper I we fail to detect dust continuum emission between W75N and the 12′-long DR21 filament. Moreover, a distance of $\sim$ 2 kpc is usually adopted for W75N, while 2–3 kpc is assumed for DR21 and DR21(OH) (Genzel & Downes 1977; Campbell et al. 1982; Fischer et al. 1985; Odenwald & Schwartz 1993). The higher value gives a more realistic population of massive stars in our analysis below, so we adopt 3 kpc as a general distance to DR21, DR21(OH) and W75N regions in this paper.

2 DATA SELECTION AND ANALYSIS

2.1 JHK Data Selection

WFCAM observations of a $0.8^\circ \times 0.8^\circ$ field, known as a WFCAM "tile", were obtained in Service Observing time at UKIRT in May and June of 2005. Data through *Mauna Kea Consortium* broad-band J, H and K filters, and through a narrow-band H_2 1-0S(1) filter were secured; the H_2 data are presented in Paper I, where the details of the WFCAM observations and data reduction are also discussed. The WFCAM field encompasses all of the region covered by the Spitzer data displayed in Fig. 1.

Catalogues of WFCAM point source photometry in the J, H and K bands were provided by the WFCAM Science archive maintained by the Cambridge Astronomical Survey Unit (CASU). JHK data were retrieved from the merged JHK catalog. The following four constraints were used when querying the catalog: a) magnitude errors of less than 0.2 mag in each band, b) a merged class identified as a star in the catalog, c) a probability that the point is a star, given by the *pStar* parameter, of greater than 0.999, and d) coordinates matched to better than 0.4″ between the JHK bands (χ and η within $\pm$0.2″ in each band). Regions of star formation contain large numbers of embedded sources which may not be visible in the J band. Therefore, the unmerged catalogs were used to obtain data in the H and K bands separately to find matching sources only in these two bands.

The JHK merged catalog with the above constraints yielded 42792 point sources in the region; the HK merged catalog contained an extra 16883 resulting in a total of 59675 sources detected in the HK bands alone. These two catalogs have been used for the photometric analysis presented in this paper. The WFCAM photometric system is based on the system of Mauna Kea Consortium Filters (Dye et al. 2006). We have maintained the same system for plotting the data points, although we have transformed the data of the reference curves (which are in Bessel-Brett system) to that of the MKO system.

2.2 Spitzer Photometry

Archival Spitzer Space Telescope data were retrieved using the Leopard software for the analysis presented here. We obtained the Post-Basic Calibrated Data (PBCD) images from two programs, namely PID-623 (IRAC Campaign W (SV-3), PI: Giovanni Fazio) and PID-1021 (DR21 and its Molecular Outflow, PI: Anthony Marston). These programs together cover almost the entire WFCAM field of view presented here and in Paper I, encompassing the DR21, W75N, the Diamond ring regions to the south west of DR21 (see Fig. 1), as well as new sites of star formation to the west of W75N, and to the west of DR21 (labeled L906E in Fig. 1 and in Paper I). Data were obtained with both the MIPS and IRAC cameras, although here we discuss only data from the latter. IRAC images in four filters, known as band 1 (band center wavelength $\sim$3.6 μm), band 2 (4.5 μm), band 3 (5.8 μm) and band 4 (8.0 μm) were obtained. The IRAC instrument is described by Fazio et al. (2004). Both programs used Full Array Readout with 2 sec exposure times. Mosaics of the individual frames were made using STARLINK routines and aperture photometry was extracted using the

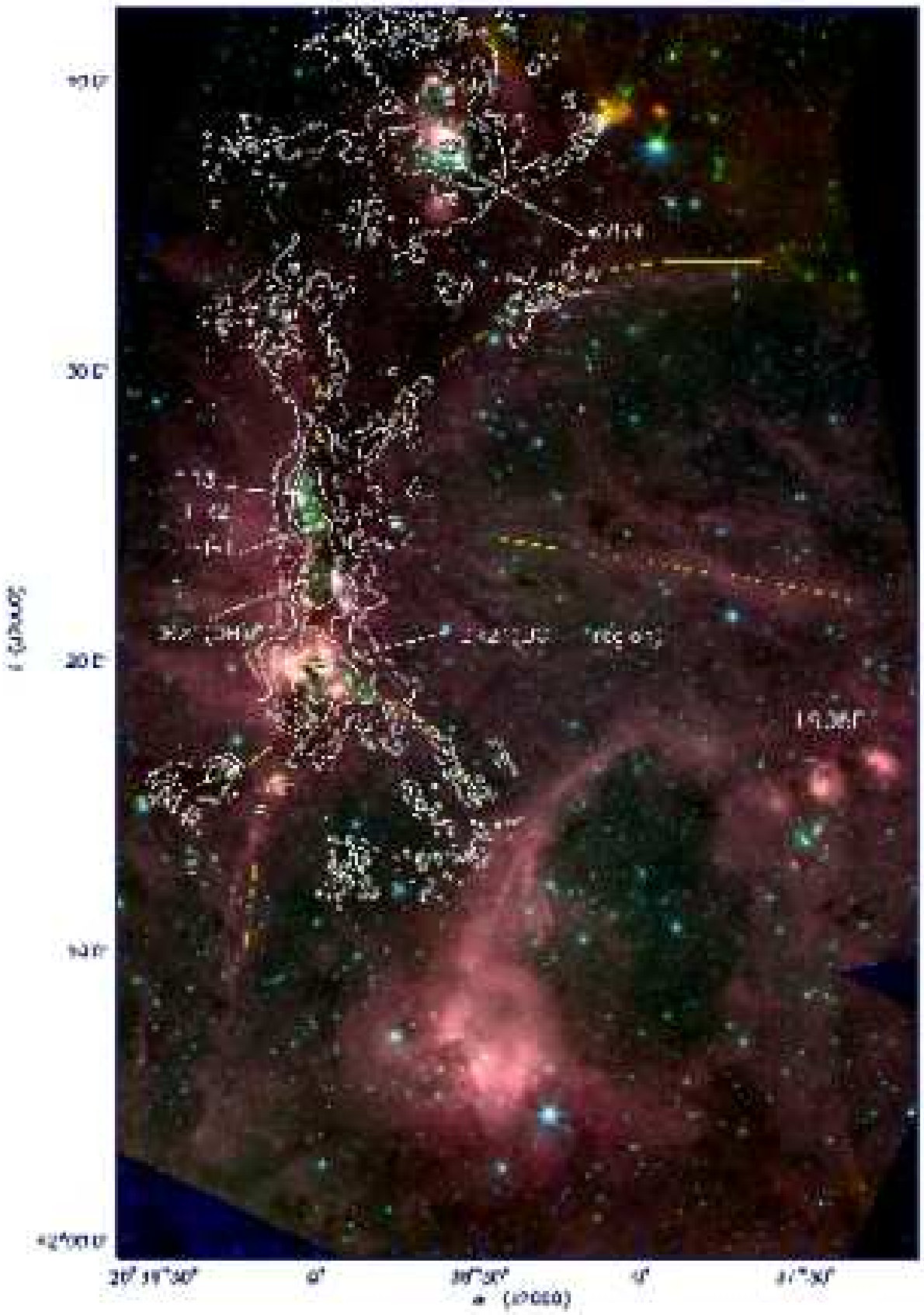

Figure 1. A colour image of the full DR21/W75 mosaic observed with the Spitzer Space Telescope, composed from images in 3.6 μm(blue), 4.5 μm(green) and 8.0 μm(red). Contours represent the 850 μm emission mapped using SCUBA on JCMT. The sketched lines are meant to indicate the large scale filamentary emission.

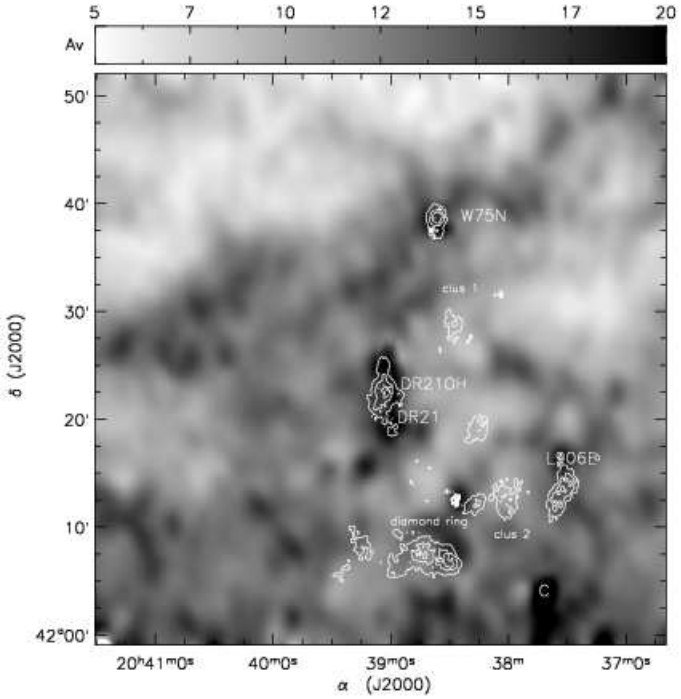

Figure 2. Near-infrared extinction map shown in grey scale. Overlaid contours represent nearest neighbour stellar density enhancements as derived from the 4.5μm IRAC image point source photometry data. The contour levels show star densities of $\sim$ 30K, 40K, 50K, 70K, 100K, 150K and 200K stars degree^{-2}

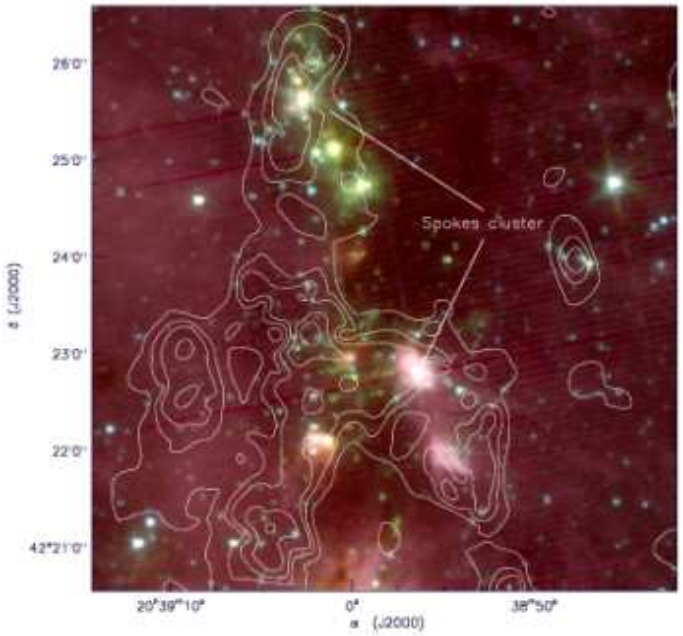

Figure 3. A zoom-in view of the region around DR21(OH) and the associated dense filament, with the three colour composite background shown in Fig. 1 overlaid by 6th nearest neighbour stellar density contours. Note the structure in clustering and the stars that form spokes cluster.

APPHOT tasks in IRAF. Images and contour plots in three of the four bands are presented in Paper I.

The PBCD fits files are calibrated in terms of MJy sr^{-1} and the photometry tasks used in *iraf* are designed to handle counts/sec. Therefore a proper conversion from the flux units to counts and estimating the photon noise is required. Photon noise was computed by using a *phpadu* (photons per image count), where $phpadu = (exptime \times gain)/(fluxconv \times pixratio)$. *exptime* is the total exposure time, *gain* is 3.3, 3.71, 3.8 and 3.8 and *fluxconv* is 0.1125, 0.1375, 0.5913 and 0.2008 for channels 1, 2, 3 and 4, respectively. The *pixratio* is the ratio between the area of the original IRAC pixels and the pixels in the mosaics. This was 1 in our case.

Aperture photometry of point sources was extracted using an aperture of 2.4″. Sky correction was applied using an inner sky annulus of 2.4″ and an outer sky annulus of 7.3″. Zero-point magnitudes corresponding to these aperture settings (including the aperture corrections) were 17.79, 17.30, 16.71 and 15.89 respectively for Channels 1, 2, 3 and 4. Using the individual photometry we then obtained matched sources between the various bands. A total of 1580 point sources were matched between all four bands. The mean photometric uncertainities are 0.02, 0.02, 0.07 and 0.15 mag for channels 1, 2, 3 and 4, respectively.

3 RESULTS

3.1 Extinction maps

In Fig. 2, the grey scale background shows the near-infrared extinction map of the region. This map was produced by Nyquist binning the spatial distribution of extinction values with a bin size of 150″. The JHK photometric data were plotted on an H-K vs J-H colour-colour diagram. In this diagram (not shown), all stars were deredenned to a locus perpendicular to the redenning vector and the vector length was measured appropriately converted to extinction values. Given the large distance to this region, the observed area is crowded by field stars redenned only by interstellar extinction. Including these field stars affects the contrast of the extinction map. Therefore, only those points with $A_v \geqslant 5$ mag were chosen to produce the extinction map shown in Fig. 2. This map traces regions of extinction between A_v of 5–30 mag, limited by the completeness limit of the WFCAM observations. However, the DR21/W75 region are associated with several dense regions with extinction greater than A_v $\sim$30 mag which do not show any stars at 2 μm, resulting in missing data points in our map. These pockets appear as white regions adjacent to the black spots (for example see the white patch adjacent to the black head of the region marked "C" in Fig. 2). Such white patches are supplemented appropriately for the portion of the field covered by SCUBA observations. This was accomplished by converting the SCUBA column densities to extinction values and an absolute calibration made by using robust extinction data points that was measured with NIR data. In those regions where SCUBA data is not available the white patches remain. A histogram of all the extinction values obtained from the WFCAM data suggest that the mean extinction to the DR21/W75N regions is A_v=6-8 mag. This is in good agreement with the value obtained by Joshi (2005) towards this line of sight within the galaxy.

The extinction map clearly traces the north-south dense

Table 1. Embedded Clusters in the mapped region

Region name	Coords (J2000)(deg) α	δ	Radius (pc) effective	core	Density (stars pc^{-2}) half-power	peak	Isoperimetric quotient	τ
W75N	309.652	42.6462	0.96	0.63	20	44	0.76	0.66
Diamond ring	309.660	42.1197	1.62	1.62	27	54	0.20	0.99
L906E	309.383	42.2238	1.24	0.91	23	49	0.45	0.73
DR21/DR21(OH)	309.767	42.3764	1.46	1.08	24	48	0.23	0.74

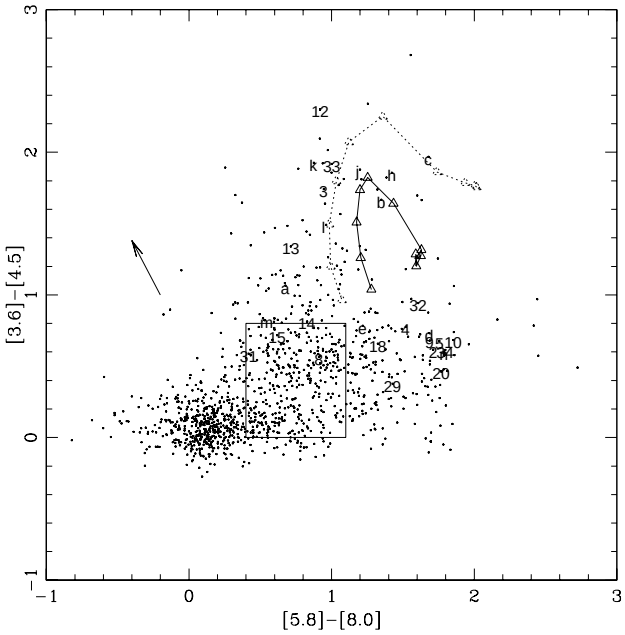

Figure 4. Colour-Colour (CC) diagram from the Spitzer IRAC data for DR21/W75, including stars associated with the Diamond Ring region and L906E. The solid box represents the region of Class II sources (Allen et al 2004). The dotted line shows synthetic fluxes for a YSO with a temperature of 32000 K; the solid curve shows a YSO track at a temperature of 15000 K (Whitney et al. 2004). Numbers and letters refer to specific sources discussed in Paper I.

molecular filament encompassing DR21, DR21-OH and the W75N region (Paper I). It also reveals other regions of high extinction towards the diamond ring cluster, L906E and region "C", which is the darkest patch in Fig. 2 extending beyond the limits of our map. It can be noted that these regions of high extinction coincide well with the brightest emission regions in the MIPS 24μm image of Marston et al. (2004) and the 850 μm dust continuum cores in Paper I. However, the Spitzer/IRAC images and 850 μm data does not encompass region "C", so the associated star formation activity is not discussed here.

3.2 Embedded Clusters

The star forming regions DR21 and W75N appear as bright near-infrared nebulae owing to illuminated gas and shock excited outflows. However, no significant stellar density enhancements are observed at 2μm (in the K band) in these regions. This means that the embedded population must be hidden inside the dense molecular cloud at higher extinction or that the YSO population is too young to be bright at 2μm. This supposition becomes obvious with the availability of IRAC images from the Spitzer Space Telescope, where many embedded YSO's are clearly visible. The contours in Fig.2 trace the embedded clusters in the region as identified by stellar density enhancements in the 4.5μm point sources. These contours were obtained by computing the 20th nearest neighbour (20NN) enhancements (Casertano & Hut 1985; Ferreira & Lada 2006) of the spatial distribution of 14,063 sources detected in this band. The clusters were detected by using the 4σ contours above the mean star counts in the region where σ is the variance of the mean star count values. Table. 1 lists the embedded clusters identified and their properties. Embedded clusters associated with DR21/DR21(OH), W75N, the diamond ring region and L906E were detected. There are a couple of fainter clusters marked clus1 and clus2 in Fig. 2 but these do not posess significant peaks, so they are not listed in Table. 1. The embedded clusters are found to be spatially coincident with the high extinction regions revealed by the extinction map obtained from the near-infrared WFCAM data. In fact, the observed clusters are better aligned with the whitish patches which represent missing data points in the near-infrared extinction map. The DR21/DR21(OH) cluster also aligns well towards one edge of the dense filament traced by the 850 μm emission.

The 4 σ contour was used to identify the boundary of the cluster, its effective radius and isoperimetric quotient. To compute the peak positions, core and half-power densities and the τ parameter we made use of a 20NN map. Table. 1 lists effective radius, peak and average stellar densities, and the τ parameter for the clusters. The effective radius is computed by measuring the area A enclosed by the 4 σ contour and computing R=$\sqrt{A/\pi}$. In Figure. 3 we show contours of a 6NN map to demonstrate the structure within the clusters; it can be noted that the clusters are elongated in the direction of the dense filament and they display significant sub-structure. Two parameters namely the isoperimetric quotient and τ are used to measure the structure of the clusters (Ferreira & Lada 2006). The isoperimetric quotient for each cluster is defined as follows: If the cluster boundary contour has a perimeter p units enclosing an area A square units, then the isoperimetric quotient of this curve is $4\pi A/p^2$. It measures the ratio of the area enclosed by the cluster boundary to the area of a circle with the same perimeter. If our clusters were circular, this quotient will be equal to 1. τ is defined as the ratio of the core radius to the effective radius and measures how much of the cluster population is in the core and how much is in the halo. Ferreira & Lada (2006) defines a cluster as heirarchical if τ

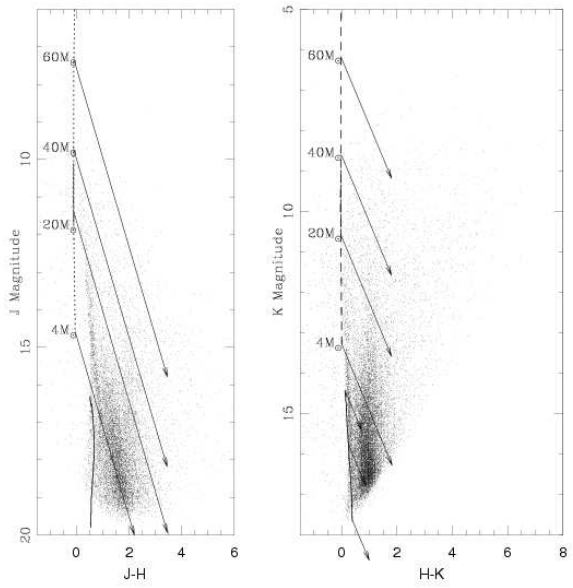

Figure 5. Colour magnitude diagrams from near-infrared JHK data. In both panels, points represent data derived from WFCAM photometry. The solid line shows 1Myr old PMS model track from Baraffe et al., the dotted line represents the 3Myr old ZAMS track from Geneva models and the solid arrows represent redenning vectors of $A_v = 30$ mag.

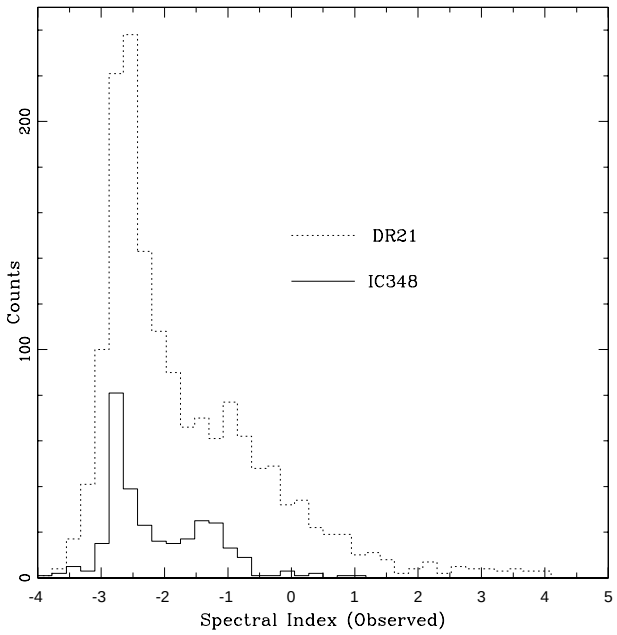

Figure 6. A histogram of spectral indices measured from linear least-squared fits to source photometry in the four IRAC bands. Thus, only sources detected in all four bands are plotted. A similar plot is presented for the IC348 Spitzer observations of Lada et al. (2006) for comparision.

is greater than 0.455. The last two columns in Table. 1 lists the isoperimetric quotient and τ values for each cluster. It can be noted that the DR21 and diamond ring clusters are the most elongated and heirarchical, while the W75N cluster is the most circular and centrally condensed.

3.3 Color-Color(CC) and Color-Magnitude(CM) diagrams

The nature of the embedded young stellar population can be evaluated using the photometric data plotted on colour-colour (CC) and colour-magnitude (CM) diagrams. The majority of the embedded population is bright in the IRAC bands. Therefore, the 1,592 point sources matched between all four IRAC bands were used to plot the IRAC CC and CM diagrams. Fig. 4 shows a [5.8-8.0] vs [3.6-4.5] CC diagram. The numbers and letters in these plots refer to specific targets that are discussed in detail in Paper I: the numbers are bright 8.0 μm point sources, often compact clusters and/or luminous sources in the region, while the letters are candidate outflow driving sources. Almost all exhibit colours consistent with protostars. In Fig. 4 the redenning vector is shown with an arrow, the two curves represent Class I models for two different temperatures (Whitney et al. 2004). The dotted curve represents the colours of a Class I YSO at a temperature of 32000 K for various inclination angles, and the solid line is a similar object at a temperature of 15000 K. The square box represents the zone of Class II objects as discussed by Allen et al. (2004). The concentrated circular distribution of points to the lower-left of the square box represents the pure photospheres. Fig. 4 shows that about 50% of the point sources detected in the IRAC bands are pure photospheres, while the remaining are distributed in the zones representative of younger objects such as Class 0, I and II (Allen et al. 2004; Megeath et al. 2004). Notice the few points with excess red colours that occupy the upper right-hand regions of the plot, i.e. regions redder than the model curves of 15 K and 32 K Class I source. These are representative of candidate massive stars.

Although the JHK data do not show any significant embedded clusters, they do reveal several embedded sources and the majority of the halo population distributed outside the densest regions of the molecular cloud. Also, the higher spatial resolution of the near-infrared data can separate multiple components (when these are present) among the embedded population. As mentioned earlier, the JHK merged catalog contains ∼43,000 sources and ∼60,000 sources in the H and K bands alone. These points are plotted on two CM diagrams shown in Fig. 5. The pre-main-sequence models of Baraffe et al. (1998) (solid line) and the zero-age-main-sequence model tracks from the *Geneva Observatory* stellar models (dotted line)(Lejeune & Schaerer 2001) are plotted for reference. The observed points were compared to model data with ages between 1 Myr–3 Myr and distances ranging between 2–3 kpc. We find that the near-infrared data are matched relatively well for an age of 3 Myr and a distance of 3 kpc. Note that the age of 3 Myr applies only to the population of stars detected in the NIR JHK bands; it does not apply to the deeply embedded population revealed by the IRAC data. The YSO population traced by IRAC data consists largely of younger objects, with an age of perhaps 1 Myr or less.

3.4 Spectral indicies of the embedded population

The IRAC bands are well suited to measuring the infrared excess emission that can be attributed to circumstellar envelopes and disks. The IRAC band fluxes have been successfully used to determine the disk excess objects and obtain reliable estimates of the disk fraction in nearby low mass star forming regions such as IC348 (Lada et al. 2006) . Lada et al. (2006) show that the pure photospheres and the disk excess sources clearly separate out when the IRAC fluxes are used to estimate the power law index of the observed spectral energy distribution. This is because the disk emission dominates in the 4.5-8.0μm, where the SED's will significantly deviate from the pure photospheres of low mass stars. A simple least squares linear fit to the observed SED between 3.6μm and 8.0μm was obtained for all of the 1,580 sources found in all four IRAC bands. Table. 2 (available online) lists the magnitudes in the four bands and the computed spectral indices. The SED's were not deredenned before fitting because an accurate estimate of the A_v to each source is possible only by fitting model atmospheres. This can not be done with the limited data available for this region.

A histogram of the observed spectral indicies α for all sources detected in the four IRAC bands in DR21/W75 is shown in Fig. 6. For comparision we also plot the indices measured for IRAC sources observed in the low mass star forming region, IC348, as described by Lada et al. (2006). DR21/W75N is located at 3 kpc resulting in a large line-of-sight extinction that will stretch the α values. Extinction due to a fixed column density of gas and dust is a function of wavelength which will attenuate the shorter wavelengths much more than the longer wavelengths. This will result in an artificial rise in the slope of the spectral energy distribution if the foreground extinction is significant, resulting in a higher value of α. However, the change is larger for sources with lower α and relatively smaller for sources with higher α thus causing a stretching of the α values rather than a simple increase. We therefore corrected the IRAC magnitudes for such effects by using the standard extinction law (Mathis 1990) and assuming an uniform foreground extinction value of Av=9 mag. Note, however, that it does not correct the actual extinction to each source which is due to the molecular cores or disks. In DR21/W75, the observed spectral indicies range from -4.0 to +4.3. The histogram for IC348 shows a prominent peak at α $\sim$-2.7, which corresponds to pure photospheres, and a somewhat less prominent peak at α $\sim$-1.8, corresponding to sources with thick disks (Lada et al. 2006). Similar peaks can be seen for the DR21 data as well, the shapes of both histograms compare quite well, representing similar aspects of star formation in both regions. However, the histogram for DR21 deviates from that of IC348 at α values greater than 0 and particularly beyond 2. A small, but significant fraction of sources in DR21 are found to have high spectral indicies, between 2 and 4.5. The higher values of α is not merely an effect of the stretching effect explained above due to high density regions. The high α sources are better represent the source functions because the change $\delta\alpha$ is smaller for high α sources compared to low α sources. We shall discuss the implications of this result in the next section.

In Fig. 7 we show the spatial distribution of the IRAC point sources using circular symbols. Sources with α >3 are shown by cross marks. The size of each symbol is proportional to the observed spectral index of the corresponding source. The background greyscale image is a 4.5μm mosaic image of the region. Sources with the highest spectral index are concentrated in the densest regions associated with the north-south molecular ridge that runs through DR21 (see Fig. 1), W75N, L906E in the west-south-west, and the Diamond Ring region. In particular, strong clustering of sources can be noticed around DR21, DR21OH, W75N and L906E region (see Fig. 1 and Fig. 7). These clusters are connected by a distributed population of sources with high spectral indices, that can be found spread along two filaments, one running north-south and the other towards the south-east and north-west. A general correlation of the disk sources with the dark patches in the entire field can be seen in Fig. 7.

4 DISCUSSION

We have explored the stellar population in and around two major, luminous ($\sim$ $10^5 L_\odot$ Moore et al. 1988; Campbell et al. 1982) star forming regions, namely DR21 and W75N, using wide field UKIRT/WFCAM JHK and Spitzer/IRAC 3.6, 4.5, 5.8 and 8.0μm images. The observed area encompasses several luminous far-infrared sources, clusters of UCHII regions (Torrelles et al. 1997; Cyganowski et al. 2003), sites of intense maser activity (Plambeck & Menten 1990; Mangum, Wooten & Mundy 1992; Hunter et al. 1994; Kogan & Slysh 1998; Torrelles et al. 1997) and powerful molecular outflows (Garden et al. 1991; Davis, Smith & Moriarty-Schieven 1998), all of which are signposts of massive star formation. The estimated distance to all these sources is more or less the same; the analysis of the data presented in Sec. 3.3 suggests a distance of $\sim$3 kpc, which is in good agreement with other estimates derived from various methods (Genzel & Downes 1977; Campbell et al. 1982; Fischer et al. 1985; Odenwald & Schwartz 1993).

The results presented in the previous section demonstrate that the DR21, DR21(OH) and W75N regions contain young stellar objects that can be classified as Class 0/I or Class II, based on Spitzer colours and spectral indices. This implies that star formation is a recent phenomenon in all of these regions. The majority of the young stellar population in each area is so deeply embedded that it is not uncovered in observations at wavelengths shortward of 2μm. The SCUBA 850 μm cores described in Paper I and shown here in Fig. 1 probably represent an evolutionary phase that is earlier even than that traced here with Spitzer. The SCUBA cores (32 are identified in Paper I) are typically not associated with 8.0 μm sources. They are generally confined to a narrow, north-south filament in DR21, and to a compact region around W75N. The Spitzer YSOs, though also certainly clustered around the dense cores and filaments, are none-the-less somewhat more widely distributed. This could be due to the displacement of YSOs away from the central density peaks as they evolve. Even so, the different epochs of star formation traced by WFCAM, Spitzer and SCUBA all seem to be co-existing in DR21/W75. Moreover, common trends such as distance, YSO class and estimated age suggest that the individual sites of star formation – W75N,

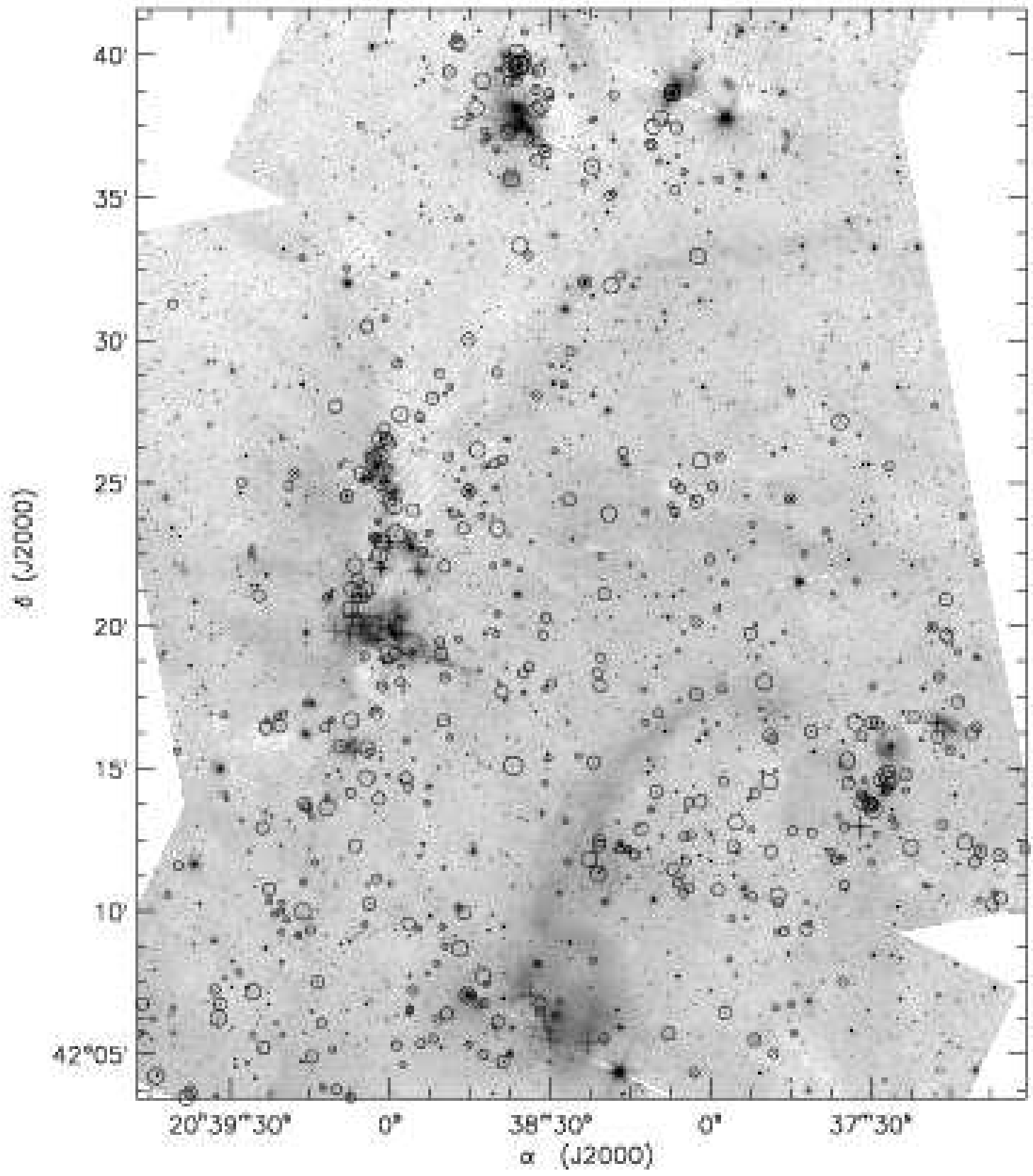

Figure 7. Distribution of infrared excess sources. IRAC channel 2 image is shown in grey scale and the circular symbols represent the excess sources. Crosses represent sources with $\alpha > 3$. The size of the symbols are proportional to the value of the spectral index.

DR21, DR21(OH), the Diamond Ring and L906E – may be connected in a global way. In the following we shall argue that there is more evidence to support this scenario.

The 8μm channel of the IRAC instrument traces warm dust and emission from PAHs (polycyclic aromatic hydrocarbons) much more efficiently than the shorter wavelength bands. The colour image of the entire region shown in Fig. 1 displays prominent filamentary nebulae. At least five long filaments of nebulosity (marked by the sketched lines in Fig. 1) can be identified in the observed region, four of which converge on the DR21/DR21OH regions. Note that the bases of these filaments are traced to some extent even in the 850 μm emission, showing that the filaments are indeed made of dense gas. We have seen from Fig. 7 that a visibly prominent distribution of thick disk sources is concentrated along the thickest filament coinciding with the DR21, DR21OH and FIR 1/2/3 regions, although the W75N region is well away from these filaments and appears disconnected. A careful examination of the same figure will also show that two other filaments that originate at DR21 and run towards the northwest and a third directly westward of DR21 are also correlated with the distribution of thick disk sources. The thin filament running directly westward of DR21 and linked to the outflow may be due to the outflow punching out of the filament. While the correlation of embedded YSOs and filaments is prominent for the filaments converging on DR21, the same is not true for the diamond ring region. The diamond ring region has a bright filament running northwards that curves toward the L906E region marked in Fig. 1. The YSOs in Fig. 7 all appear to be concentrated in the L906E region and just below the filament, rather than at the head of the diamond ring. This suggests that the diamond ring region is relatively evolved, while L906E is actively forming young stars. Note that no H_2 jets were discovered near the diamond ring, while a number of flows were identified around L906E (Paper I). A proper analysis of the filaments and their relative orientation requires additional mapping at 850 μm (our SCUBA map does not extend as far south as the diamond ring, or as far west as L906E) and CO line data with good spatial and velocity resolution.

As shown in section. 3.2, embedded clusters are associated with each of the main targets in the region, namely DR21/DR21(OH), W75N, L906E and the diamond ring region. The clusters show cores on scales of $\sim$1 pc. If each cluster peak represents a molecular clump out of which the clusters were born, then the size scales of the cluster cores represent the scales of fragmentation in this filamentary cloud. The main DR21 filament traced by the 850 μm emission is about 16 pc long and is one of the most structured filaments in terms of embedded clusters. A zoom-in view of this region is shown in Fig. 3 along with contours of the stellar density. The contours display multiple stellar density peaks. These clusters are elongated roughly along the north-south filament. In this figure notice the bright stars marked as "Spokes Clusters", which include the FIR 1/2/3 850 μm peaks (refer Fig. 1) in one line. Each of these bright stars are surrounded by a noticeable linear alignment of fainter stars that are arranged like the spokes of a wheel whose centre coincides with the bright star. This type of structure has been recently identified by Teixeira et al. (2006) in NGC2264, which is at a somewhat closer distance of d=800 pc, and is therefore more clearly visible. These authors show that the linearly aligned fainter stars are indeed redder than the central luminous source. Such structures are thought to be important because they represent primordial structures in the formation of a star cluster representing true proto-clusters (Kurosawa et al. 2004; Bate et al. 2003). Although the spokes configuration in the clusters shown in Fig. 3 are not as prominent as that shown by Teixeira et al. (2006) (possibly due to the larger distance of DR21), there are never-the-less four such clusters in DR21. The association of these clusters with bright 850 μm emission and a young population of stars with high spectral indicies indicates that this region may represent multiple adjacently located protoclusters.

The filamentary structures found in the DR21/W75 region on the scales of giant molecular clouds (16-20 pc), and those found on smaller scales, such as the "spokes clusters", collectively resemble the pattern predicted by the numerical simulations of Bate et al. (2003). The simulations by Bate et al. (2003) are made for a 50$M_\odot$ cloud, which is much smaller than the actual mass of the DR21/W75 clouds. However, qualitatively, their results seem to be applicable even here, suggesting that the mechanism of gravo-turbulent star formation effectively operates on the scales of giant molecular clouds, up to several hundred thousand solar masses and several parsecs in dimension. The filamentary nature appears heirarchical if we consider the smaller scale spokes configurations and the larger scale filaments feeding on to the center of the DR21/DR21(OH) region. This heirarchy can be carefully observed by comparing structures in Fig. 1 and Fig. 3.

Finally, we mention the implications of the sources with high α values in DR21 distributed along the dense filament and also coinciding with sign-posts of massive star formation. α >2 in a simplistic interpretation implies presence of Class 0 objects. Recently, Robitaille et al. (2006) presented and discussed a large grid of 200,000 YSO model SEDs. According to their work, there are a number of reasons why α (measured in the Spitzer IRAC bands) can assume high values: a) younger sources such as Class 0 sources are known to have high α, b) higher mass accretion rate and/or larger disk/envelope masses boost α, and c) beyond 5000K, α will increase with the temperature of the star, due to a lower contribution from the stellar flux and a higher contribution from the infrared dust spectrum. In DR21/W75N the observed data points satisfy almost all of the above conditions because they are situated in the densest parts of the star forming region, they coincide with sign-posts of massive star formation such as UCHII region and water masers, and because they occupy the colour zone of Class 0 protostars on a CC diagram. More quantitative comparisions of the real nature of massive stars requires the plotting of data from theoretical SEDs on to CM diagrams. However, in colour-colour space there is significant overlap of data points for the different evolutionary states, source masses, temperatures, disks and even inclination angles (Robitaille et al. 2006), particularly if one uses a limited number of photometric bands. Rigorous comparisions will require multiple wavelength observations, particularly at larger wavelengths such as 24 μm and 100 μm where younger and luminous objects are known to particularly bright.

5 CONCLUSIONS

We analyse NIR and MIR point-source photometry over an area that includes the massive star forming regions DR21, DR21(OH), and W75N, as well as recently-discovered clusters of more evolved young stars (the Diamond Ring region), and bok-globule-like cores where low mass stars are probably forming (L906E). We use colour-colour and colour-magnitude diagrams, as well as extinction maps and surface density plots, to examine the population of young stars across the region. We also measure the MIR spectral index for 1580 sources.

Our extinction map traces much of the clumpy, north-south filament associated with DR21 and DR21(OH), as well as new cores that may be associated with separate episodes of star formation. The very densest cores, however, are not extracted from the NIR data, because of extinction larger than A_v ∼30 mag.

NIR and MIR color-colour and colour-magnitude plots show that the JHK and 4.5 μm–8.0 μm data trace different YSO populations, as expected: the WFCAM data reveal sources with ages of ∼1–3 Myr, and mostly present in a widespread halo, while the IRAC point sources are clustered along the dense filaments traced by 850 μm data. Spectral indices for the Spitzer sources indicate a more embedded and/or massive population in DR21/W75 than is seen in the IC348 low-mass star forming region. There is a significant fraction of sources with indices greater than 2 and up to 4 in DR21/W75. Indeed, ∼40% of the Spitzer-detected sources in the field have SEDs consistent with Class 0/I or Class II YSOs. The reddest sources are generally associated with the densest cores, as traced in 850 μm dust continuum emission in Paper I, or in 8.0 μm PAH emission. The NIR data, tracing the evolved and halo YSOs represent a ~ 3 Myr old population whereas the Spitzer data, tracing the more deeply embedded content and also associated with outflow activity, represents a relatively younger population of 1 Myr or less.

Star formation in DR21 region is found to be occuring in filaments of 10-20 pc lengths that is fragmented in to multiple clusters on the scales of 1-2 pc. We identify four spokes cluster configurations in the main DR21 filament that is representative of proto-clusters. The morphological appearance on the scales of the entire Giant Molecular Cloud resembles well the numerical simulations of cluster formation by Bate et al. (2003).

6 ACKNOWLEDGMENTS

MSNK greatfully acknowledges Paula Teixeira for helpful discussions on Spitzer photometry. We also thank an anonymous referee for useful suggestions and a speedy review. MSNK and JMCG are supported by a grant POCTI/CFE-AST/55691/2004 and JMCG is supported by a grant SFRH/BD/21624/2005 approved by FCT and POCTI, with funds from the European community programme FEDER. DF received funding from the CosmoGrid project, funded by the Program for Research in Third Level Institutions under the National Development Plan and with assistance from the European Regional Development Fund. This research made use of data products from the Spitzer Space Telescope Archive. These data products are provided by the services of the Infrared Science Archive operated by the Infrared Processing and Analysis Center/California Institute of Technology, funded by the National Aeronautics and Space Administration and the National Science Foundation. Finally, we would like to thank the team at CASU for processing the NIR data, and the WFCAM Science Archive in Edinburgh for making the data available to us.

REFERENCES

Allen L.E. et al., 2004, ApJS, 154, 363
Baraffe, I., Chabrier, G., Allard, F., Hauschildt, P. H. 1998, A&A, 337, 403
Bate, M. R., Bonnell, I. A., Bromm, V. 2003, MNRAS, 339, 577
Campbell M.F., Hoffman W.F., Thronson H.A., Hiles D., Nawfel R., Hawrylyca M., 1982, ApJ, 261, 550
Casertano S., Hut P., 1985, ApJ, 298, 80
Chandler C.J., Gear W.K., Chini R., 1993, MNRAS, 260, 337
Cyganowski C.J., Reid M.J., Fish V.L., Ho P.T.P., 2003, ApJ, 596, 344
Davis C.J., Kumar M.S.N., Sandell G., Froebrich D., Smith M.D., Currie M.J., 2006, MNRAS, submitted (Paper I).
Davis C.J., Smith M.D., 1996, A&A, 310, 961
Davis C.J., Smith M.D., Moriarty-Schieven G.H., 1998, MNRAS 299, 826
Dickel J.R., Dickel H.R., Wilson W.J., 1978, 223, 840
Dye S., et al., 2006, MNRAS, in press
Fazio G.G., et al., 2004 ApJS, 154, 10
Ferreira, B., Lada, E. A. 2006, in preparation
Fischer J., Sanders D.B., Simon M., Solomon P.M., 1985, ApJ, 293, 508
Garden R.P., Hayashi M., Gatley I., Hasegawa T., Kaifu N., 1991, ApJ, 374, 540
Genzel R., Downes D., 1977, A&AS, 30, 145
Harvey, P. M., Campbell, M. F., Hoffmann, W. F. 1977, ApJ, 211, 786
Harvey, P. M., Chapman, N., Lai, Shih-Ping., Evans, Neal. J., II et al, 2006, ApJ, 644, 307
Haschick A.D., Reid M.J., Burke B.F., Moran J.M., Miller G., 1981, ApJ, 244, 76
Hunter T.R., Taylor G.B., Felli M., Tofani G., 1994, A&A, 284, 215
Irwin M., et al., 2006 in prep.
Jorgensen, J. K., Harvey, P. M., Evans, N. J., II, Huard, T. L., Allen, L. E., et al. 2006, ApJ, 645, 1246
Joshi 2005, MNRAS, 362, 1259
Kogan L., Slysh V., 1998, ApJ, 497, 800
Keto, E. R. 1990, ApJ, 350, 722
Kurosawa, R., Harries, T. J., Bate, M. R., Symington, N. H. 2004, MNRAS, 351, 1134
Lada, C.J., Muench, A.A., Luhman, K.L., et al. 2006, AJ, 131, 1574
Lejeune, T., Schaerer, D. 2001
Mangum J.G., Wooten A., Mundy L.G., 1992, ApJ, 388, 467
Marston A.P. et al., 2004, ApJS, 154, 333.
Mathis, J. S. 1990, ARA&A, 28, 37
Megeath S.T. et al., 2004, ApJS, 154, 367

Moore T.J.T., Mountain C.M., Yamashita T., McLean I.S., 1991, MNRAS, 248, 377
Moore T.J.T., Mountain C.M., Yamashita T., Selby M.J., 1988, MNRAS, 234, 95 W75N photom
Persi P., Tapia M., Smith H.A., 2006, A&A, 445, 971
Robitaille T.P., Whitney B.A., Indebetouw R., Wood K., Denzmore, P. 2006, ApJ, accepted.
Odenwald S.F., Schwartz P.R., 1993, ApJ, 405, 706
Plambeck R.L., Menten K.M., 1990, ApJ, 364, 555
Shepherd D.S., Testi L., Stark D.P., 2003, ApJ, 584, 882
Shirley Y.L., Evans N.J., Young K.E., Knez C., Jaffe D.T., 2003, ApJS, 149, 375
Smith H.A., et al., 2005, In: Proceedings of the dusty and molecular universe: a prelude to Herschel and ALMA, ed. A. Wilson, ESA SP-577, ESA Publications Division, p.197
Teixeira, P., Lada, C. J., Young, E. T., et al. 2006, ApJ, 636, L45
Torrelles J.M., Gomez J.F., Rodriguez L.F., Ho P.T.P., Curiel, S., Vazquez R., 1997, 489, 744
Vallée J.P., Fiege J.D., 2006, ApJ, 636, 332
Whitney, B.A., Indebetouw, R., Bjorkman, J.E., Kenneth, W. 2004, ApJ, 617, 1177
Wilson T.L., Mauersberger R., 1990, A&A, 239, 305